Acta Materialia 191 (2020) 51–59

Contents lists available at ScienceDirect

Acta Materialia

journal homepage: www.elsevier.com/locate/actamat

Full length article

Regulation of phase transition and magnetocaloric effect by ferroelectric domains in FeRh/PMN-PT heterojunctions

Kaiming Qiao[a,b,1], Jianlin Wang[a,b,1], Fengxia Hu[a,b,c,*], Jia Li[a,b], Cheng Zhang[a,b], Yao Liu[a,b], Zibing Yu[a,b], Yihong Gao[a,b], Jian Su[a,b], Feiran Shen[a,b], Houbo Zhou[a,b], Xuedong Bai[a,b,c], Jing Wang[a,b,d,*], Victorino Franco[e], Jirong Sun[a,b,c], Baogen Shen[a,b,c,*]

[a] Beijing National Laboratory for Condensed Matter Physics, Institute of Physics, Chinese Academy of Sciences, Beijing 100190, PR China
[b] School of Physical Sciences, University of Chinese Academy of Sciences, Beijing 100049, PR China
[c] Songshan Lake Materials Laboratory, Dongguan, Guangdong 523808, PR China
[d] Fujian Innovation Academy, Chinese Academy of Sciences, Fuzhou, Fujian 350108, PR China
[e] Dpto. Física de la Materia Condensada, ICMSE-CSIC, Universidad de Sevilla, P.O. Box 1065, 41080 Sevilla, Spain

ARTICLE INFO

Article History:
Received 24 December 2019
Revised 29 February 2020
Accepted 19 March 2020
Available online 8 April 2020

Keywords:
FeRh film
Regulation of phase transition
Magnetocaloric effect
Ferroelectric domains

ABSTRACT

The narrow temperature span, ΔT_{span}, of first-order magnetocaloric materials is a serious problem that limits the application as refrigerants. Here we report tunable phase transition and magnetocaloric effect controlled by ferroelectric (FE) domains in FeRh films grown on (001)- and (011)-cut PMN-PT substrates. Adjacent two-step phase transition, and hence significantly broadened ΔT_{span}, has been achieved in FeRh films by utilizing the multi-domain structure of PMN-PT substrates. The results of aberration corrected (ac)-STEM, EELS and EDX analysis revealed that a 3~4 nm buffer layer with AB_2O_4-type spinel structure is naturally formed at the interface, which largely reduces the lattice mismatch between FeRh and PMN-PT and plays a key role for the successful growth of epitaxial (oriented) FeRh film on either (001)- or (011)-oriented PMN-PT. The switched FE domains by electric field govern the phase transition of FeRh films. As a result, regulated entropy change and refrigeration capacity in a wide temperature span have been achieved. On this basis, a feasible magnetic refrigeration cycle facilitated by electric field is designed. The present study provides an experimental basis for expanding the refrigeration temperature span by ferroelectric domain engineering, which is significant for promoting refrigeration application of first-order magnetocaloric materials particularly in micro-devices.

1. Introduction

Ozone layer destruction and high energy consumption caused by conventional gas compression refrigeration is becoming serious. Increasing demands for energy-saving and environmental friendliness calls for solid-state refrigeration technology [1–10]. Looking for materials with large caloric effect in a wide temperature span is the primary concern for the realization of solid-state refrigeration. The materials with first-order phase transition are usually considered to be ideal solid-state refrigerants owing to the significant magnetocaloric effect (MCE) [6–9], elastocaloric effect [3,4] and barocaloric effect [10]. However, the narrow temperature span originated from the sharp phase transition is one of the recognized problems hindering its application [11]. Unremitting efforts have been made to broaden the cooling temperature span, such as introducing chemical pressure [12–14], hydrostatic and uniaxial pressure [15,16]. Moreover, nanostructuring was also proposed to be an effective way to broaden temperature span and enhance refrigeration capacity [17]. However, most studies focused on bulk samples. Thin film has more extensive applications and richer physical properties due to its size effects [18] and coupling with substrate [19]. In particular, with the increasing demands for refrigeration in microelectronic circuits, the miniaturization of refrigeration devices has become an urgent task.

FeRh is a giant magnetocaloric material discovered in early years [20], which is suitably fabricated into epitaxial thin film since its lattice matches with a lot of single crystalline substrates. However, the thin films of FeRh still show first-order transition and the MCE behavior is similar to that of bulk. Equiatomic FeRh alloy with cubic structure undergoes a first-order transition from antiferromagnetic (AFM) to ferromagnetic (FM) state accompanying with 1% volume expansion [20], which makes it sensitive to external fields such as magnetic field [21] or strain [22]. Any mismatch between film and substrate can produce static strain, which will modify the phase transition and MCE. Moreover, for the FeRh films grown on ferroelectric (FE)

* Corresponding authors at: Beijing National Laboratory for Condensed Matter Physics, Institute of Physics, Chinese Academy of Sciences, Beijing 100190, PR China.
E-mail addresses: fxhu@iphy.ac.cn (F. Hu), wangjing@iphy.ac.cn (J. Wang), shenbg@iphy.ac.cn (B. Shen).
[1] Both the authors contributed equally to this work.

https://doi.org/10.1016/j.actamat.2020.03.028
1359-6454/

substrate, a dynamic strain caused by FE domain switching can be introduced under cyclic electric field besides the common static strain due to lattice mismatch. As a result, the phase transition and MCE can be dynamically regulated.

Here, the relaxor ferroelectric single crystals (1-x)Pb($Mg_{1/3}Nb_{2/3}$)O_3-x$PbTiO_3$ (x = 0.3) (PMN-PT) with (001) and (011) orientations were chosen as substrates to grow FeRh films. The rhombohedral (R) PMN-PT has 8 spontaneous polarization FE domains along body diagonals, and the vector projections in the same crystal plane are different with each other due to the asymmetrical R structure [23,24]. The subtle difference of static strains caused by the different FE domains can make the phase transition of FeRh films split. Additionally, the FE domain switching (109°, 71°, 180°) [25–27] and structural transition (rhombohedral-tetragonal R-T [28], or rhombohedral-orthogonal R-O [29]) driven by electric field can change both the proportion of FE domains and lattice parameters of PMN-PT substrate, and the concomitant strains all exert on the FeRh films. The combined actions of static and dynamic strains governed by the FE domains can significantly broaden phase transition and lead to rich MCE behavior.

To disclose the epitaxial relationship and growth mechanism of the FeRh films on the different (001)- and (011)-oriented PMN-PT, spherical aberration corrected transmission electron microscopy (ac-STEM), electron energy loss spectroscopy (EELS), as well as energy dispersive x-ray spectroscopy (EDX) analysis were performed to examine the microstructures and distinguish element distributions. The results indicate that a 3~4 nm buffer layer with AB_2O_4 type spinel structure is naturally formed at the interface, which largely reduces the lattice mismatch between FeRh and PMN-PT and plays a key role for the epitaxial growth of FeRh films on either (001)- or (011)-oriented PMN-PT. The formation and orientations of the AB_2O_4 spinel layer, as well as the epitaxial relationship across the buffer layer, were analyzed in detail for the different heterojunctions. Taking advantage of the multi-domain structure of PMN-PT substrate, FeRh films also show multi-domain coexistence and hence adjacent two-step phase transition takes place. As a result, the temperature span of phase transition is significantly broadened. Meanwhile, entropy change and refrigeration capacity can be continuously adjustable in a wide temperature span by utilizing ferroelectric domain switching and/or ferroelectric phase transition induced by electric field. On this basis, a feasible magnetic refrigeration cycle facilitated by electric field is designed.

2. Experiments

FeRh films were grown on both (001)- and (011)-oriented PMN-PT substrates at 750 °C in an argon pressure of 0.2 Pa with a power of 29 W by magnetron sputtering and in situ annealed for one hour. The structure and crystal orientations were characterized by four circle x-ray diffraction (XRD) with Cu-Kα radiation. Microstructures at the interface of FeRh/PMN-PT were examined by ac-STEM (JEM-ARM300F, JEOL Ltd) operated at 300 kV with a cold field-emission gun and double dodecapoles spherical aberration (Cs) correctors. The convergence angle was 18mrad and the angular range of collected electrons for high-angle annular dark field (HAADF) imaging was 54–220mrad. Elemental analysis by EELS and EDX was carried out to determine the distribution of elements. Au layers were vapor deposited on bottom side of FeRh/PMN-PT heterostructure as electrodes. The magnetic properties were measured using a superconducting quantum interference device (SQUID–VSM) with in situ electric fields applied across the FeRh/PMN-PT structure by a Keithley 6517B electrometer. The leakage current is below 5nA under a 6 kV/cm electric field.

3. Results and discussion

3.1. Crystal structure of FeRh films grown on (001)- and (011)-oriented PMN-PT substrates

Fig. 1a and b shows the XRD patterns of FeRh films grown on (001)- and (011)-oriented PMN-PT substrates, respectively. It can be seen that the FeRh film grown on (001)-PMN-PT orients along [011] direction while the one on (011)-PMN-PT orients along [001] direction. According to the cube-on-cube epitaxial orientation relationship and lattice parameters of FeRh (a_{FeRh}=2.995 Å) [30] and PMN-PT (a_{PMN-PT}=4.017 Å) [31], the lattice mismatch along two in-plane directions can be deduced from $\varepsilon=\frac{a_{PMN-PT}-a_{FeRh}}{a_{PMN-PT}}$. For FeRh(011)/(001) PMN-PT, the ε along FeRh [01−1](011)||PMN-PT [100](001) and FeRh [100](011)||PMN-PT [010](001) directions are 5.42% and 25.4%, respectively. While for FeRh(001)/(011)PMN-PT, the ε along FeRh [100](001)||PMN-PT [100](011) and FeRh [010](001)||PMN-PT [01−1](011) directions are 25.4% and 5.42%, respectively. One can note that the lattice relations are completely the same for FeRh(011)/(001)PMN-PT and FeRh(001)/(011)PMN-PT, indicating that the same growth mode may be adopted for both heterojunctions. Such a large lattice mismatch will cause the accumulation of strain energy and make the lattice unstable [32]. Moreover, for the cubic FeRh film grown on rhombic (001) and (011) plane with an angle of α=89.9° of PMN-PT single crystal [25], as shown in Fig. 1c and d, lattice distortion will occur during the growth, which also leads to the instability of FeRh lattice [32].

To disclose the epitaxial relationship and growth mechanism, ac-STEM analysis was performed to analyze the microstructures of FeRh/PMN-PT. HAADF image of FeRh(001)/(011)PMN-PT is shown in Fig. 1f. It can be seen that a buffer layer with a thickness of ~3.7 nm is naturally formed at the interface, and the structure is identified to be AB_2O_4 type spinel with c-axis along [001] while in-plane a-axis is along [110] direction. The corresponding atomic arrangements of α-FeRh, spinel buffer layer, and PMN-PT are schematically depicted on the right panel of HAADF image (Fig. 1f). The weaker contrast of the buffer layer compared with film and substrate in the HAADF image is caused by the thinner thickness of buffer layer, the ion milling speed of which is faster than that of the film/substrate. It can be noted that, in the HAADF image, the brightness of the four rhombic vertex atoms in the buffer layer is much larger than in other positions, consistent with the AB_2O_4 type spinel structure, noting that the number of atoms in the four rhombic vertices is twice as much as in other positions in the structure [33]. To further explore the formation mechanism of buffer layer, the elemental distributions at the interface were analyzed by both EDX and EELS spectroscopy. EDX is good at distinguishing heavy elements while EELS has a better resolution for light elements [34]. It can be seen, from Fig. 1g, that Fe atoms not only appear in the FeRh film but also distribute in the entire buffer layer. However, Pb atoms only appear in the substrate but not in the buffer layer (Fig. 1h). From Figure S1b-f, one can find that the buffer layer also contains Ti, Mg, Nb, O without Rh elements. That is to say, the buffer layer contains all elements except Pb in the PMN-PT substrate, and also contains Fe. Although we are unable to distinguish the exact elements locating at A and B positions at the moment (possibly random occupation), the AB_2O_4 type spinel structure is clear for the buffer layer. Moreover, it is reasonable to speculate the formation process of spinel structure by considering the volatile characteristics of Pb. Pb atoms on the surface layers of PMN-PT volatilize during film growth and cause Pb vacancies. The Fe atoms from the FeRh film infiltrate into the interface, promoting the formation of the spinel buffer layer, as shown in Fig. 1l.

For FeRh(001)/(011)PMN-PT, the epitaxial relationship through the interfaces can be identified from the HAADF image shown in

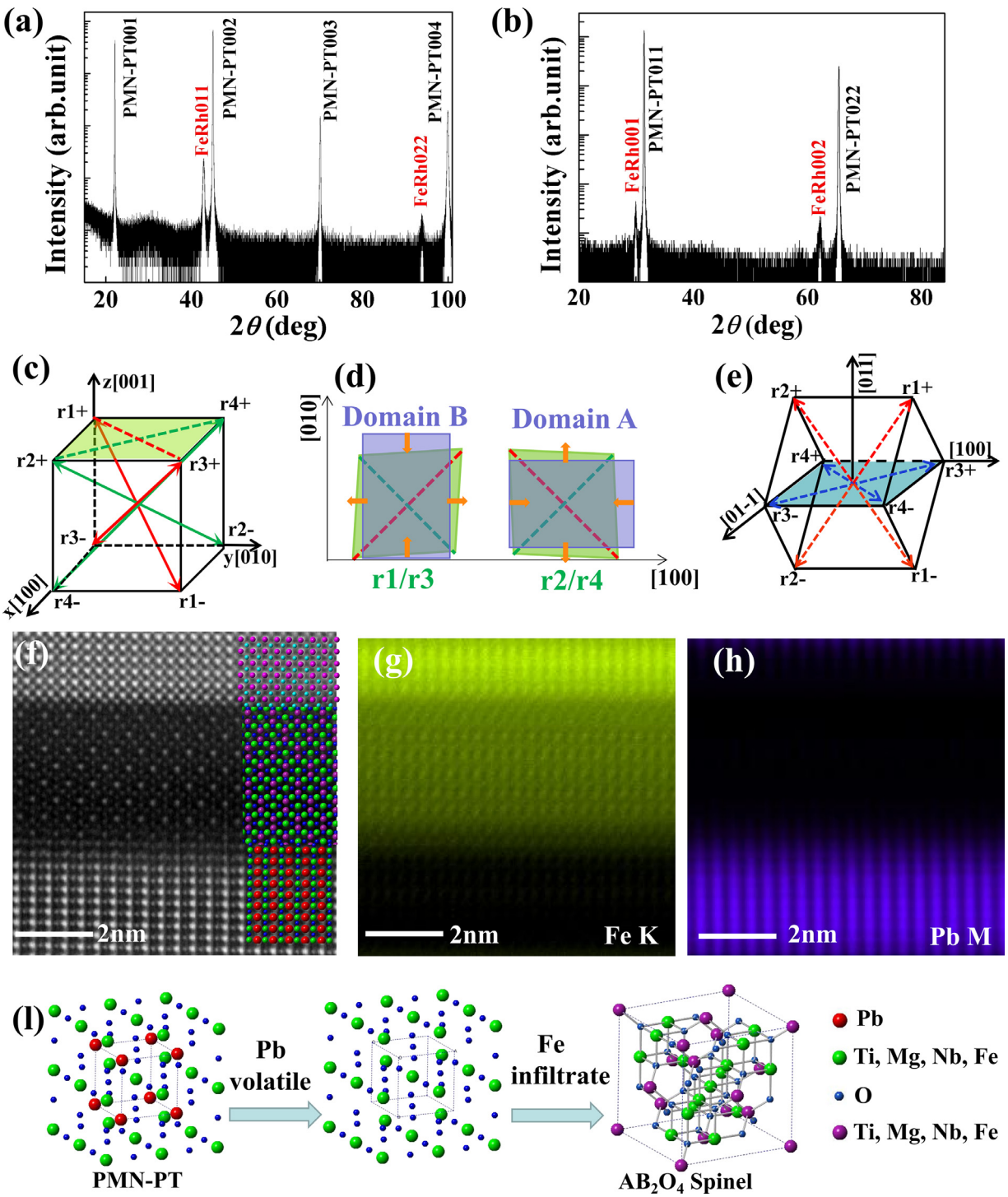

Fig. 1. The XRD patterns of (a) FeRh(011)/(001)PMN-PT and (b) FeRh(001)/(011)PMN-PT heterostructure at room temperature; (c) Configuration of spontaneous polarization vectors along body diagonals shown by arrows for (001)-oriented PMN-PT single crystal and (d) the projections of ferroelectric domains r1/r3 and r2/r4 in the (001)-plane and the corresponding FeRh domains in (011)-plane; (e) Configuration of spontaneous polarization vectors along body diagonals shown by arrows for (011)-oriented PMN-PT single crystal; (f) Cross-sectional STEM HAADF image of FeRh(001)/(011)PMN-PT heterostructure and the corresponding atomic arrangement of α-FeRh, buffer layer and PMN-PT; EDX mapping of (g) Fe (green) and (h) Pb (purple) element distribution at the interface, where the scale bar is 2 nm in length; (l) Schematic diagram of spinel buffer layer formation. Pb atoms (red) in the ABO_3 perovskite PMN-PT volatilize at high temperature, and Pb vacancies appear, which give rise to the skewing of adjacent atoms. During film growth, Fe atoms at the interface permeate into Pb vacancies, facilitating the formation of a buffer layer with spinel structure. (For interpretation of the references to color in this figure legend, the reader is referred to the web version of this article.)

Fig. 1f, where the atomic arrangement model is displayed on the right panel. The lattice mismatch among the FeRh film, the buffer layer and the PMN-PT substrate can be evaluated by referencing lattice parameters of the bulk (FeRh: 2.995 Å, spinel: 8.454 Å [35], PMN-PT: 4.017 Å), though the actual strain is hard to be obtained for each layer. At the interface of (011)PMN-PT/(001)spinel, two spinel unit cells along [110] match well with three PMN-PT unit cells along [100], and the lattice mismatch produces a tensile strain about +0.77% on the spinel layer. At the interface of (001)FeRh/(001)buffer layer, two FeRh unit cells along [100] direction match with one spinel

unit cell along [110], and the lattice mismatch produces a compressive strain about −0.18% on the FeRh film. This analysis indicates that the direct large mismatch between FeRh(001) and (011)PMN-PT is significantly reduced by the formation of spinel layer, which facilitates the epitaxial growth of FeRh film. The good epitaxial growth of film can help effective transmission of strain from substrates, particularly for the strain produced by FE domains. It was reported that the strain produced by piezoelectric stress can propagate over a long distance of 600 nm while the strain remains unchanged [36,37].

Similarly, a ~4 nm buffer layer with AB_2O_4 type spinel structure was also detected in the interface of FeRh(011)/(001)PMN-PT. Although the area of buffer layer is unclear in the HAADF image (Figure S2a,c) compared to that between FeRh(001)/(011)PMN-PT (Fig. 1e) because of its thinner thickness caused by preparation, the similar spinel structure can be identified from the ABF image (Figure S2b and d) fortunately, where the *c*-axis of the buffer layer is along [001] direction while the in-plane *a*-axis is along [100] (see supplementary material S2). Besides the spinel buffer layer, multi-domain structure was detected in the FeRh film. As shown in Figure S2, two kinds of domains appear in FeRh, which have the same out-of-plane orientation along [011], but the in-plane orientation is different. The one along in-plane [01−1] is labeled as domain A (Figure S2a and b) while the other along in-plane [100] labeled as domain B (Figure S2c and d). Such occurrence of multi-domain structure of FeRh film is closely related to the FE multi-domain in PMN-PT substrates. For the (001) cut PMN-PT, the projections of FE domains r1/r3 (r1+r1-r3+r3-) in the (001)-plane are the same, but different from the projections of FE domains r2/r4(r2+r2-r4+r4-) in the same plane. Both are rhombus with the same side length, but rotated by 90° with each other, as shown in Fig. 1d. For the (011) oriented FeRh film on the rhombus (001) plane of PMN-PT, the rectangular FeRh lattice will twist and deform. To release the strain energy and distortion energy, two kinds of domains alternately grow. The one with [100] side in (011)-plane of FeRh film along the [100] direction of r1/r3 FE domain corresponds to domain B, while the one with [01−1] side in (011)-plane of FeRh film along the [100] direction of r2/r4 FE domain corresponds to domain A. For both domains, the epitaxial relationships with substrates can be deduced similarly to the case of FeRh(001)/(011)PMN-PT by referencing lattice parameters of the bulk. At the interface of (001)PMN-PT/(001)spinel, 10 spinel unit cells along [100] match with 21 PMN-PT unit cells along [100], and the lattice mismatch produces a compressive strain about −0.20% on the spinel layer. At the interface of (011)FeRh/(001)spinel, for domain A, four FeRh unit cells along [01−1] match with one spinel unit cell along [100], and a compressive strain about −0.21% is produced on the FeRh film; while for domain B, 14 FeRh unit cells along [100] match with 5 spinel unit cells along [100], and a tensile strain about +0.8% is generated on the FeRh film. The coexistence of domains A and B undergoing different strains will lead to successive two-step phase transition in FeRh films (Fig. 2).

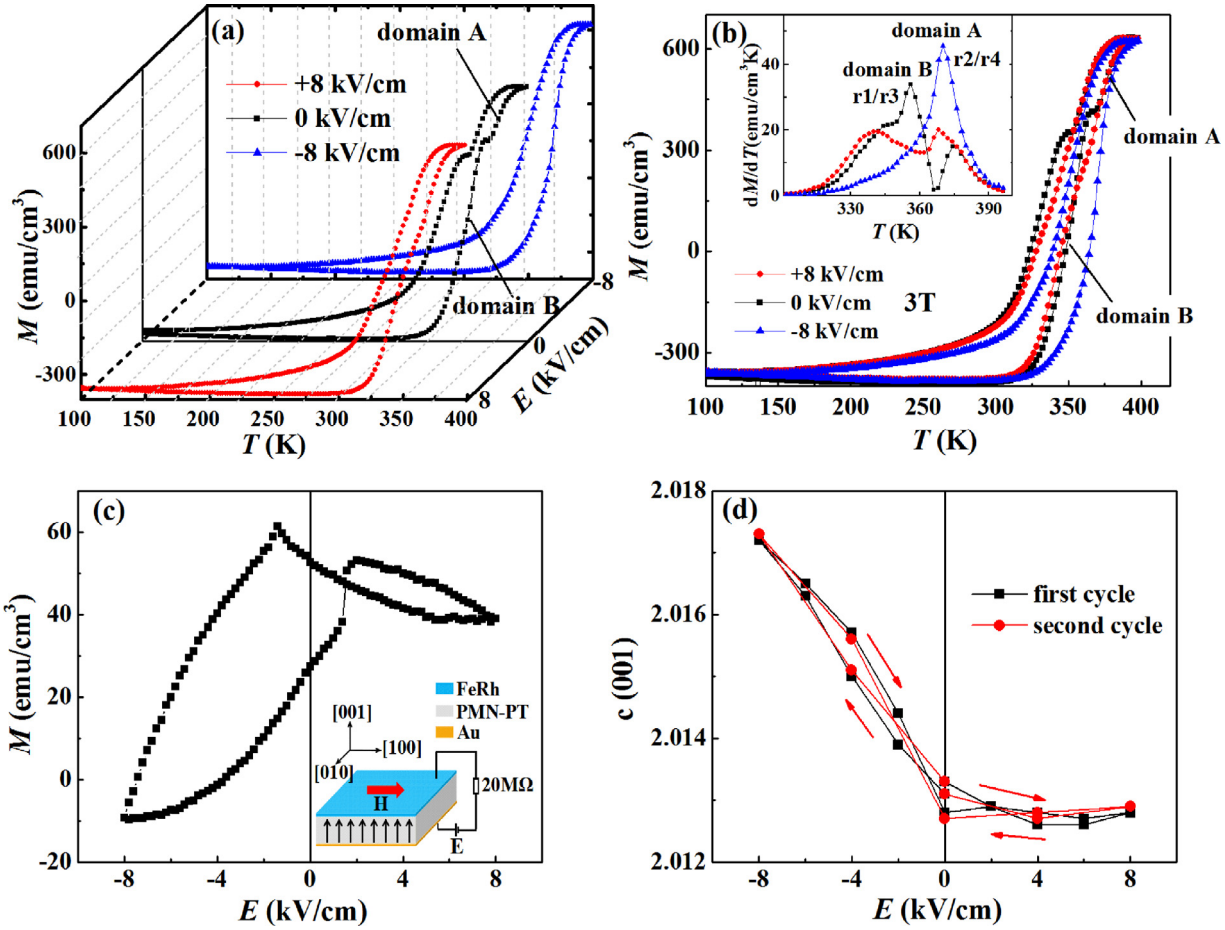

Fig. 2. Temperature dependence of magnetization (*M-T* curves) measured at 3T magnetic field with in situ electric field of 0 kV/cm, +8 kV/cm and −8 kV/cm. (a) three-dimensional plots, (b) two-dimensional plots, where the corresponding d*M*/d*T*-*T* in heating process is shown in the inset. (c) Electric field dependence of magnetization (*M-E* curve) measured at constant temperature 330 K and magnetic field 5T. The inset shows sketch of (011)FeRh/(001)PMN-PT heterostructure with in-situ electric field applied, where *H* and *E* represent the direction of applied magnetic field and electric field, respectively. (d) The measured out-of-plane lattice parameter of (001)PMN-PT substrate as a function of electric field. (For interpretation of the references to color in this figure, the reader is referred to the web version of this article.)

3.2. Phase transition and magnetocaloric effect controlled by ferroelectric domain switching in FeRh(011)/(001)PMN-PT

Temperature dependent magnetization (*M-T* curves) measured under 3T magnetic field is shown in Fig. 2 (black curves). Similar to the bulk, an external magnetic field can also shift the phase transition temperature to lower temperature for FeRh films. The negative magnetization in Fig. 2 originates from the diamagnetism of substrates. It can be seen that the (011) FeRh films on (001)PMN-PT undergo AFM-FM first-order phase transition, which is similar but different from that of FeRh bulk. For FeRh bulk without strain, there have been many studies on the MCE since the first report in 1990 [20]. However, the reported entropy change ΔS is always a single peak, originating from the single AFM-FM magnetoelastic transition. So, it is difficult to adjust the phase transition span. One can note, from Fig. 2, that the FeRh film exhibits consecutive two step phase transition both in heating and cooling process, which can be clearly seen from the d*M*/d*T*-*T* curve with two peaks at 356 K and 376 K on heating (black curve, inset of Fig. 2b). The occurrence of the two step transition should be related to the alternately grown domains in the FeRh films governed by FE domains r1/r3 and r2/r4 (Figure S2). For FeRh alloy, the compressive (tensile) strain can stabilize AFM (FM) phase and shift the phase transition towards high (low) temperature [38,39]. Therefore, domain A under compressive strain governed by r2/r4 domain corresponds to the high temperature part of the two-step phase transition, and domain B under tensile strain governed by r1/r3 domain corresponds to the low temperature part of the two-step phase transition. The low temperature peak in the d*M*/d*T*-*T* curve is higher than the high temperature peak. It indicates that the amount of domain B governed by r1/r3 domain is larger than that of domain A governed by r2/r4 domain, which is consistent with the result that the proportion of r1/r3 FE domain is higher than r2/r4 in the initial state of PMN-PT substrates. In particular, a bevel cut of PMN-PT can make the amount of ferroelectric domains r1/r3 more than those of r2/r4 [25,40], which is confirmed by reciprocal space maps (RSM) of the (113) reflection (see supplementary material S3).

Moreover, one can notice, from Fig. 2b, that the FeRh films display broadened transition on cooling compared to that on heating. The relative origin was studied previously, which can be ascribed to the film crystal quality, defects, and strains [41–44]. For example, Fan et al. performed polarized neutron reflectometry studies on the FeRh films grown on MgO [43]. The detected FM moment at temperatures far below the AFM-FM transition was demonstrated originating from the strains between films and substrates. Loving et al. [44] presented structural evidence for the stabilized ferromagnetism in epitaxial FeRh films on MgO, which well explained the broadened transition on cooling based on classical nucleation theory. For the AFM–FM transition on heating, the retained FM components promote the growth of the additional FM regions which then work together to align the other remaining areas, hence leading to an abrupt transition. While for the inverse FM–AFM transition on cooling, the FM regions are strongly coupled with simultaneously hampering the nucleation of AFM phase, thus resulting in a broadened cooling branch and a long tail in the *M-T* curve.

To explore the impact of ferroelectric domain switching on phase transition of (011)FeRh/(001)PMN-PT heterostructure, *M-T* curves with the same magnetic field of 3T along in-plane [100] direction were measured under electric fields of +8 and −8 kV/cm along out of plane [001] direction (see the sketch in the inset of Fig. 2c). The results and the corresponding d*M*/d*T*-*T* curves on heating are plotted in Fig. 2a,b and the inset. When the +8 kV/cm was applied, the two step transition of FeRh film still remains but the ratio between the two has changed. Domain B governed by r1/r3 reduces while Domain A by r2/r4 grows. The heights of the two peaks in the d*M*/d*T*-*T* curve (red) are nearly identical. In contrast, when the −8 kV/cm was applied, the two step transition nearly disappears and merged into a single one with position nearly the same as the Domain A at 0 kV/cm (see the single peak with a small bump on the left in the d*M*/d*T*-*T* blue curve). These results can be ascribed to the combined effect of strain induced by ferroelectric domain switching and the change of FE domain proportion. When the +8 kV/cm is applied, the proportion of r2/r4 FE domain increases due to 109° domain switching (Supporting materials S3), thus the corresponding amount of domain A governed by r2/r4 domain increases. Therefore, the heights of high temperature peak in d*M*/d*T*-*T* curve (red) increases at +8 kV/cm. Actually, 109° domain switching only covers 26% of the entire poled area, most are 71°(r1+→r3- or r3+→r1-)/180°(r1+→r1- or r3+→r3-) domain switching. No change of FE domain proportion occurs in 71°/180° domain switching, but a compressive strain will be generated. However, both the *M-E* curves and ε-*E* curves in Fig. 2c and d are asymmetrical, which may be ascribed to the inhomogeneity in composition or bevel cut of (001)-PMN-PT single crystal (Details can be seen in Supporting materials S4). Compared to 0 kV/cm, the parameter of PMN-PT keeps almost unchanged at + 8 kV/cm, namely, the corresponding strain at + 8 kV/cm is small due to the asymmetrical polarizations, and its effect on phase transition can be ignored. When the −8 kV/cm is applied, the proportion of 109° domain switching is almost the same as +8 kV/cm, which also makes the amount of domain A increase and the high temperature peak increase. Besides, a large compressive strain also generates due to the 71°/180° domain switching as shown in Fig. 2d. Thus, the phase transition temperature of domain B dominated by r1/r3 FE domains moves to high temperature, and approaches to that of domain A dominated by r2/r4 domains. At last, the two-step phase transformation merges. The small bump on the left in the d*M*/d*T*-*T* curve may be due to the uncompleted FE domain switching (see Supplement material S3).

To study the effect of FE domain switching on the magnetocaloric effect of FeRh film, isothermal magnetization curves were measured using loop method [45] under different electric fields for FeRh(011)/(001)PMN-PT. The calculated entropy changes (ΔS) based on Maxwell relationship are shown in Fig. 3. It can be seen that two ΔS peaks appear under 0 kV/cm due to the double domain structure of the FeRh film. The low temperature peak contributed by domain B is higher than the high temperature one contributed by domain A (Fig. 3a), which agrees with the *M-T* and the corresponding *dM/dT-T* curves (black, Fig. 2). The low and high temperature ΔS peaks at 347.5 K and 377.5 K have maximum values about 108 mJ/cm^{3}K and 77 mJ/cm^{3}K for a magnetic field change of 0–5T, respectively (Table 1). With FE domain switching induced by electric field, these two ΔS peaks evolve to be nearly identical in height at +8 kV/cm (Fig. 3c) while they merge into a single one with a small bump on the left at −8 kV/cm (Fig. 3b). All these behaviors completely agree with the *M-T* and *dM/dT-T* curves (red and blue, Fig. 2). Table 1 summarizes the peak position, peak value, full width at half maximum (FWHM) of ΔS-*T* curves, refrigeration capacity (*RC*). *RC* is an important parameter to evaluate the performance of MCE material, i.e. the energy that a refrigerant can transfer between hot and cold reservoirs. It can be determined from $RC = \int_{T_2}^{T_1} |\Delta S(T)|_{\Delta H} dT$, where T_1 and T_2 refer to the temperatures corresponding to the full width at half maximum (FWHM) in the $|\Delta S_M(T)|$ curves [46]. It is noticeable that the modification of RC by the application of electric field does not alter significantly the magnitude of the peak ΔS when an appropriate electric field was chosen. Moreover, Griffith et al. recently raised another reasonable parameter to evaluate the MCE material [47], namely temperature averaged entropy change (TEC), $TEC(\Delta T_{lift}) = \frac{1}{\Delta T_{lift}} \max_{T_{mid}} \left\{ \int_{T_{mid}-\frac{\Delta T_{lift}}{2}}^{T_{mid}+\frac{\Delta T_{lift}}{2}} \Delta S_M(T) dT \right\}$, where ΔT_{lift} refers to the desired lift temperature in response to a given field change. Here we choose ΔT_{lift} ~10 K to evaluate the TEC(10 K) while T_{mid} is obtained by sweeping over the available $\Delta S(T)$ data and selecting

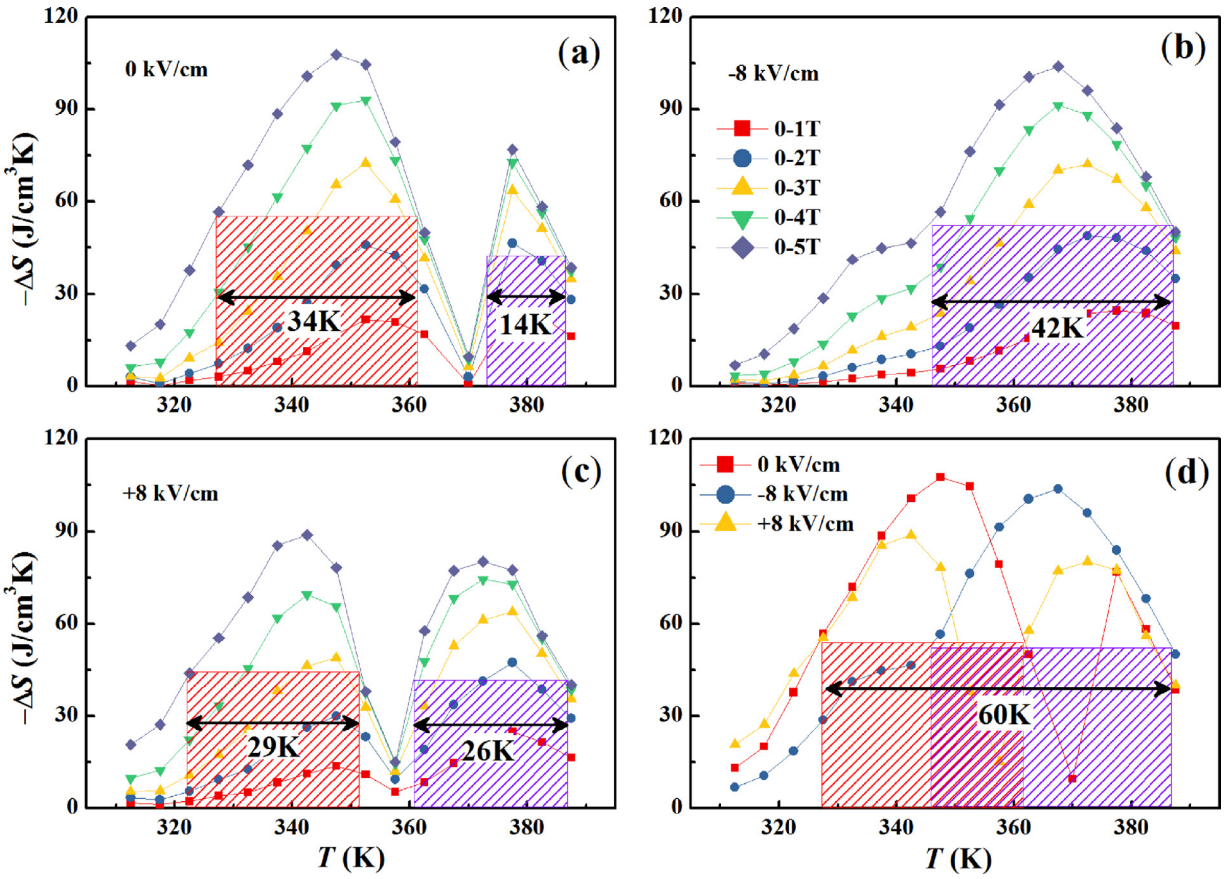

Fig. 3. Entropy change (ΔS) as a function of temperature and magnetic field for FeRh(011)/(001)PMN-PT under electric fields (a) 0 kV/cm, (b) −8 kV/cm, (c) +8 kV/cm. (d) The comparison of ΔS curves at 0−5T under 0 kV/cm, −8 kV/cm and +8 kV/cm, where the corresponding refrigeration temperature spans are marked.

Table 1
Magnetic refrigeration parameters (0−5T) of FeRh(011)/(001)PMN-PT at different electric fields.

Electric field (kV/cm)	0		+8		−8	
ΔS peak	Low temperature	High temperature	Low temperature	High temperature	Low temperature	High temperature
ΔS peak position(K)	347.5	377.5	342.5	372.5	337.5	367.5
ΔS peak value (mJ/cm^{3}K)	108	77	89	80	45	104
FWHM(K)	34	14	29	28		42
RC(mJ/cm^3)	2976	836	2055	1772	466	3494
TEC(10 K) at the peak position (mJ/cm^{3}K)	103	63	85	79	45	101
RC_{total} covering all (mJ/cm^3)	3812		3827		3960	

the value that maximizes TEC(ΔT_{lift}) for the given ΔT_{lift} [47]. The obtained TEC(10 K) is also listed in Table 1. The performance of TEC for the present films is comparatively attractive [47].

It can be seen from Table 1 that the FWHM of ΔS-T curves can be largely adjusted by the FE domain switching induced by electric field, thereby the RC of FeRh film. For example, the available cooling temperature span can be dynamically widened from 34 K (327K-361 K) to 60 K (327K-387 K) by tuning E from 0 to −8 kV/cm. It is almost doubled, as shown in Fig. 3d. Although there is no significant change in the total RC_{total} covering the two ΔS peaks of FeRh film, the relative magnitude of the two in different temperature regions can be effectively regulated by the electric field. In particular, the appearance of two adjacent ΔS peaks with nearly equal height under +8 kV/cm suggests that the FeRh films can be simultaneously applied in the corresponding two temperature regions.

3.3. Phase transition and magnetocaloric effect controlled by ferroelectric R-O phase transition in FeRh(001)/(011)PMN-PT

Due to the multidomain structure of substrate, FeRh films grown on (011)-oriented PMN-PT substrate also show two step phase transition, which can be seen from the M-T and corresponding dM/dT-T curves (black) measured at 0 kV/cm and 0.5 T (Fig. 4b and its inset). The sketch of the circuit applying electric field and magnetic field is shown in Fig. 4a. From the dM/dT-T curves, the two step phase transition under 0 kV/cm is located at 368 K and 378 K. The origin is the same as that in (011)FeRh/(001)PMN-PT. The different projections of ferroelectric domains r1/r2 and r3/r4 in the (011) plane of PMN-PT substrate makes the FeRh films grow in two kinds of domains, which undergo different in-plane strains owing to lattice mismatch. When an electric field (+6 kV/cm or −6 kV/cm) is applied across the thickness direction of (011)-PMN-PT substrate, the multidomain

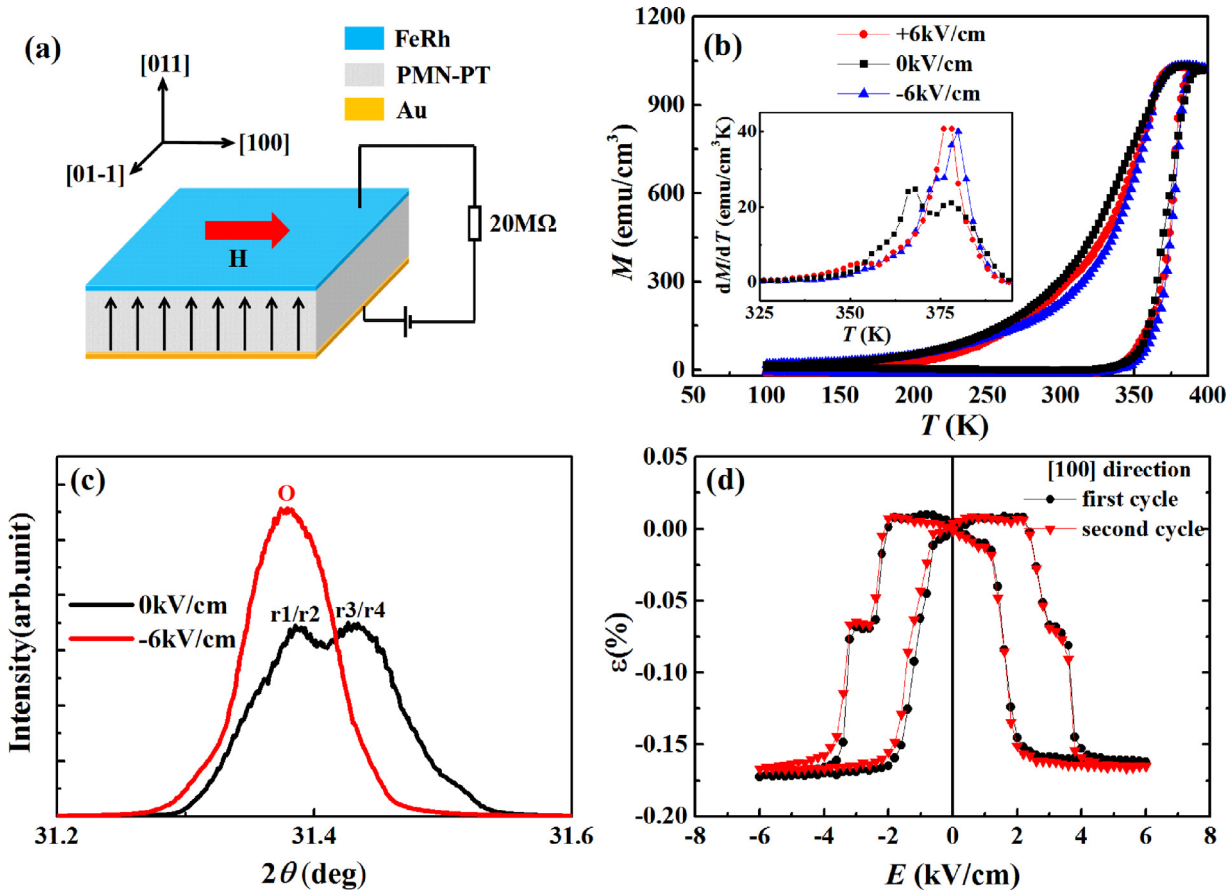

Fig. 4. (a) Sketch of (001)FeRh/(011)PMN-PT heterostructure with in-situ electric field applied, where *H* and *E* represent the direction of applied magnetic field and electric field, respectively. (b) *M-T* curves of (001)FeRh/(011)PMN-PT at different electric fields at 0.5 T. Inset shows the corresponding d*M*/d*T*-*T* curves on heating. (c) XRD patterns of PMN-PT substrate collected under 0 kV/cm and - 6 kV/cm at room temperature. (d) Strain as a function of electric field (*ε*-*E* curve) along in-plane [100] direction measured by strain gauge at room temperature.

rhombohedral phase transforms into a single domain orthogonal phase (R-O phase transition) and a compressive strain along in-plane [100] direction is produced (Supplement material S4). As a response, the two step phase transition of FeRh films merges into a single one and moves to higher temperature (inset of Fig. 4b).

To evidence the R-O phase transition of (011)PMN-PT substrate driven by electric field, XRD patterns under different in situ electric fields were collected at room temperature. The results are shown in Fig. 4c. Under 0 kV/cm, the observed two peaks correspond to the coexisting multidomain structure r1/r2 and r3/r4 in R phase, from which the calculated out-of-plane projections of lattice parameters are 5.696 Å and 5.687 Å, respectively. These values are consistent with those reported previously [27]. When the −6 kV/cm is applied, the two peaks merge into a single one and moves to a lower angle, corresponding to a single domain orthogonal phase [48]. Meanwhile, the in-plane parameter along [100] compresses, which favors AFM phase of FeRh film and shifts the phase transition to higher temperature. All these agree well with the behaviors of *M-T* and *dM/dT-T* curves (inset of Fig. 4b). However, the multi-domain structure of (001)FeRh film governed by r1/r2 and r3/r4 FE domains was not observed in the STEM image, which can be understandable considering the isotropic atomic configuration in both in-plane and out-of-plane directions for the (001)-oriented FeRh film. Note that the difference in the out-of-plane projections of lattice parameters between r1/r2 and r3/r4 is rather small, only 0.01 Å. The corresponding response in FeRh films is hard to be distinguished from the STEM image.

Moreover, the strain as a function of electric field (*ε*-*E* curves) was measured along the in-plane [100] direction of (011)-PMN-PT substrate by strain gauges (Fig. 4d). The *ε*-*E* curves are nearly symmetrical for positive and negative electric fields and no obvious offset of the coercive electric field is observed, which is coincident with the *M-T* curves at ±6 kV/cm. The occurrence of symmetrical strain curves in (011)-oriented PMN-PT substrate might be due to the more homogeneous composition than that of (001)-oriented PMN-PT. The produced compressive strain is about ~ −0.18% under either +6 kV/cm or −6 kV/cm. Repeated measurements demonstrate good repeatability, as shown by the consistence of first and second cycles in Fig. 4d.

To study the effect of electric field driven R-O phase transition on magnetocaloric effect, isothermal magnetization curves were measured under 0 kV/cm and −6 kV/cm, and the calculated Δ*S*-*T* curves based on Maxwell relation are plotted in Fig. 5. As expected, two peaks appear under 0 kV/cm, which originates from the multi-domain structure of FeRh film governed by FE domains r1/r2 and r3/r4 as stated above. The low and high temperature *ΔS* peaks at 347.5 K and 367.5 K with maximum about 142 mJ/cm^{3}K and 74 mJ/cm^{3}K for a magnetic field change of 0–5T, respectively. When the −6 kV/cm was applied, the two *ΔS* peaks merged into a single one, consistent with the *M-T*, d*M*/d*T*-*T* curves (Fig. 4b and its inset) and the XRD results (Fig. 4d). The single Δ*S* peak locates at 357.5 K with maximum about 153 mJ/cm^{3}K at 0–5T. This Δ*S* value is about 8% higher than that of low temperature Δ*S* at 0 kV/cm. Additionally, the FWHM of Δ*S*-*T* curve at −6 kV/cm is 33 K, widened by 8 K with respect to the FWHM (25 K) of the low temperature Δ*S* peak at 0 kV/cm. According to the Δ*S* peak value and FWHM, RC is 3151 mJ/cm^3 and 827 mJ/cm^3 for the low and high temperature Δ*S* peak at 0 kV/cm, respectively. The total RC_{total} covering the two peaks is 3978 mJ/cm^3 at 0 kV/cm while the RC_{total} covering a single peak at −6 kV/cm

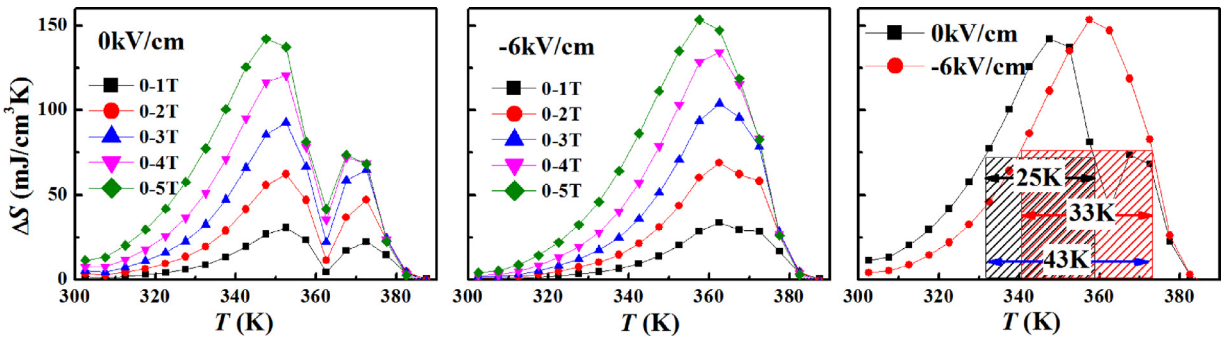

Fig. 5. Entropy change (ΔS) as a function of temperature and magnetic field for (001)FeRh/(011)PMN-PT under electric fields (a) 0 kV/cm, (b) −6 kV/cm. (c) The comparison of ΔS curves at 0–5T under 0 kV/cm, −6 kV/cm, where the corresponding refrigeration temperature spans are marked.

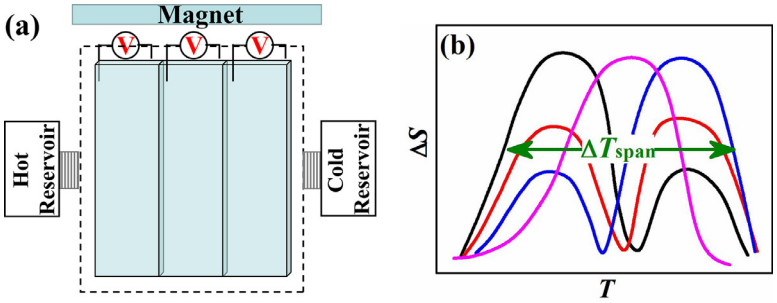

Fig. 6. (a) Schematic diagram of dual field stimulated AMR cycle; (b) The ΔS-T curves of FeRh layer tuning by FE domains of PMN-PT substrates.

is 3995 mJ/cm^3. However, the electric field regulation can enable the RC and ΔS to be distributed or concentrated at different temperature regions to meet specific requirements. The available cooling temperature span of FeRh film can be widened from 25 K (331K-356 K) to 43 K (331K-374 K) by utilizing the R-O phase transition induced by electric field, as shown in Fig. 5c.

3.4. Design of AMR cycle based on the regulated phase transition and magnetocaloric effect by ferroelectric domain

The active regenerative magnetic refrigeration (AMR) [49] has been regarded as an alternative refrigeration cycle with high energy efficiency compared to conventional refrigeration techniques. Magnetocaloric materials with first-order transition usually have narrow temperature span. To achieve refrigeration in a wide temperature span, composite of multiple materials with different transition temperatures is usually required [11,50], properly arranged in the refrigerator bed. However, phase transition characteristics are usually sensitive to preparation arts particularly for the first-order materials, which make it difficult to prepare materials with continuous phase transitions. Based on the regulated phase transition and magnetocaloric effect by ferroelectric domain in FeRh/PMN-PT heterojunctions, a feasible AMR cycle with assistance of electric fields can be designed, as shown in Fig. 6a.

The material beds of the AMR cycle can consist of FeRh films on (001) and (011) PMN-PT substrates. The entropy change for all cases is shown in Fig. 6b. For the FeRh(011)/(001)PMN-PT, two separated ΔS peaks already appear in a broadened temperature region in the absence of electric field (black curve in Fig. 6b). Application of proper electric field can adjust the magnitude of ΔS and RC through switching FE domains in the corresponding temperature regions (red and blue curves in Fig. 6b). Meanwhile, the ΔS peak of FeRh(001)/(011) PMN-PT (magenta curve) can complements the temperature range between the two separated ΔS peaks of FeRh(011)/(001)PMN-PT. Then good refrigeration performance can be realized in a continuously wide temperature span and the peak positions can be dynamically adjusted by regulating the applied electric field depending on the working conditions of the refrigerator at each moment. This dynamic control could be used as an additional parameter for the optimization of the device.

4. Conclusion

In conclusion, adjacent two-step phase transition in FeRh films has been realized and hence the working temperature span ΔT_{span} of FeRh films was greatly broadened by utilizing the alternatively arranged two kinds of domains in FeRh films induced by multi-domain in PMN-PT substrates. The growth mechanism is confirmed by STEM. A 4 nm thick spinel buffer layer naturally formed at the interface greatly reduces the lattice distortion and lattice mismatch. The two step phase transition can also be regulated by FE domain switching or FE phase transition. As a result, a continuously adjustable ΔS and RC in a wide temperature span is achieved, which solves the key problem of narrow working temperature span in first order MCE materials. On this basis, a dual field stimulated AMR cycle based on the ferroelectric domain controlled MCE is proposed. This work provides an effective way to broaden the available cooling temperature span by utilizing ferroelectric domains and simultaneously solves difficult problems of the material preparation which provide a solid foundation for the application of first-order phase transition material films in micro/nano devices.

Declaration of Competing Interest

The authors declare that they have no known competing financial interests or personal relationships that could have appeared to influence the work reported in this paper.

Acknowledgments

This work was supported by the National Key Research and Development Program of China (2017YFB0702702, 2019YFA0704904,

2018YFA0305704, 2017YFA0206300, 2017YFA0303601, 2016YFB0700903), the National Natural Sciences Foundation of China (U1832219, 51531008, 51771223, 51590880, 51971240, 11674378, 11934016, 11921004), the Strategic Priority Research Program (B) and key program of the Chinese Academy of Sciences (CAS). V.F. acknowledges the support of AEI/FEDER-UE (project MAT-2016-77265-R).

Supplementary materials

Supplementary material associated with this article can be found in the online version at doi:10.1016/j.actamat.2020.03.028.

References

[1] V.K. Pecharsky, K.A. Gschneidner Jr, The giant magnetocaloric effect in $Gd_5(Si_2Ge_2)$, Phys. Rev. Lett. 78 (1997) 4494–4497.
[2] B. Neese, B. Chu, S.G. Lu, Y. Wang, E. Furman, Q.M. Zhang, Large electrocaloric effect in ferroelectric polymers near room temperature, Science 321 (2008) 821–823.
[3] L. Mañosa, A. Planes, Materials with giant mechanocaloric effects: cooling by strength, Adv. Mater. 29 (2017) 1603607.
[4] T. Jaka, E. Kurt, E. Dan, D. Stefano, T. Janez, P. Nini, A regenerative elastocaloric heat pump, Nat. Energy 1 (2016) 16134.
[5] X. Moya, S. Kar-Narayan, N.D. Mathur, Caloric materials near ferroic phase transitions, Nat. Mater. 13 (2014) 439–450.
[6] Y.Y. Gong, D.H. Wang, Q.Q. Cao, E.K. Liu, J. Liu, Y.W. Du, Electric field control of the magnetocaloric effect, Adv. Mater. 27 (2015) 801–805.
[7] J. Liu, T. Gottschall, K.P. Skokov, J.D. Moore, O. Gutfleisch, Giant magneto-caloric effect driven by structural transitions, Nat. Mater. 11 (2012) 620–626.
[8] K.M. Qiao, F.X. Hu, Y. Liu, J. Li, H. Kuang, H.R. Zhang, W.H. Liang, J. Wang, J.R. Sun, B.G. Shen, Novel reduction of hysteresis loss controlled by strain memory effect in FeRh/PMN-PT heterostructures, Nano Energy 59 (2019) 285–294.
[9] H. Zhang, A. Armstrong, P. Müllner, Effects of surface modifications on the fatigue life of unconstrained Ni-Mn-Ga single crystals in a rotating magnetic field, Acta Mater. 155 (2018) 175.
[10] L. Mañosa, D. Alonso, A. Planes, E. Bonnot, M. Barrio, J. Tamarit, S. Aksoy, M. Acet, Giant solid-state barocaloric effect in the Ni-Mn-In magnetic shape memory alloy, Nat. Mater. 9 (2010) 478–481.
[11] V. Franco, J.S. Blazquez, J.J. Ipus, J.Y. Law, L. Moreno-Ramirez, A. Conde, Magnetocaloric effect: from materials research to refrigeration devices, Prog. Mater. Sci. 93 (2018) 112–232.
[12] A.O. Pecharsky, K.A. Gschneidner Jr., V.K. Pecharsky, The giant magnetocaloric effect between 190 and 300K in the $Gd_5Si_xGe_{4-x}$ alloys for 1.4-x-2.2, J. Magn. Magn. Mater. 267 (2003) 60.
[13] A. Fujita, S. Fujieda, Y. Hasegawa, K. Fukamichi, Itinerant-electron metamagnetic transition and large magnetocaloric effects in $La(Fe_xSi_{1-x})_{13}$ compounds and their hydrides, Phys. Rev. B 67 (2003) 104416.
[14] B.G. Shen, J.R. Sun, F.X. Hu, H.W. Zhang, Z.H. Cheng, Recent progress in exploring magnetocaloric materials, Adv. Mater. 21 (2009) 4545–4564.
[15] E. Stern-Taulats, A. Planes, P. Lloveras, M. Barrio, J.L. Tamarit, S. Pramanick, S. Majumdar, C. Frontera, L. Mañosa, Barocaloric and magnetocaloric effects in $Fe_{49}Rh_{51}$, Phys. Rev. B 89 (2014) 214105.
[16] S.A. Nikitin, G. Myalikgulyev, M.P. Annaorazov, A.L. Tyurin, R.W. Myndyev, S.A. Akopyan, Giant elastocaloric effect in FeRh alloy, Phys. Lett. A 171 (1992) 234–236.
[17] A. Biswas, S. Chandra, M.H. Phan, H. Srikanth, Magnetocaloric properties of nanocrystalline $LaMnO_3$: enhancement of refrigerant capacity and relative cooling power, J. Alloys Compd. 545 (2012) 157–161.
[18] V. Uhlır, J.A. Arregi, E.E. Fullerton, Colossal magnetic phase transition asymmetry in mesoscale FeRh stripes, Nat. Commun. 7 (2016) 13113.
[19] S. Maat, J.U. Thiele, Eric E. Fullerton, Temperature and field hysteresis of the antiferromagnetic-to-ferromagnetic phase transition in epitaxial FeRh films, Phys. Rev. B 72 (2005) 214432.
[20] S.A. Nikitin, G. Myalikgulyev, A.M. Tishin, M.P. Annaorazov, K.A. Asatryan, A.L. Tyurin, The magnetocaloric effect in Fe49Rh51 compound, Phys. Lett. A 148 (1990) 363–366.
[21] A. Chirkova, K.P. Skokov, L. Schultz, N.V. Baranov, O. Gutfleisch, T.G. Woodcock, Giant adiabatic temperature change in FeRh alloys evidenced by direct measurements under cyclic conditions, Acta Mater. 106 (2016) 15–21.
[22] C. Bordel, J. Juraszek, D.W. Cooke, C. Baldasseroni, S. Mankovsky, J. Minar, H. Ebert, S. Moyerman, E.E. Fullerton, F. Hellman, Fe spin reorientation across the metamagnetic transition in strained FeRh thin films, Phys. Rev. Lett. 109 (2012) 117201.
[23] H.X. Fu, R.E. Cohen, Polarization rotation mechanism for ultrahigh electromechanical response in single-crystal piezoelectrics, Nature 403 (2000) 281–283.
[24] G.S. Xu, H.S. Luo, H.Q. Xu, Z.W. Yin, Third ferroelectric phase in pmnt single crystals near the morphotropic phase boundary composition, Phys. Rev. B Condens. Matter Mater. Phys. 64 (2001) 020102.
[25] S. Zhang, Y.G. Zhao, P.S. Li, J.J. Yang, S. Rizwan, J.X. Zhang, J. Seidel, T.L. Qu, Y.J. Yang, Z.L. Luo, Q. He, T. Zou, Q.P. Chen, J.W. Wang, L.F. Yang, Y. Sun, Y.Z. Wu, X. Xiao, X.F. Jin, J. Huang, C. Gao, X.F. Han, R. Ramesh, Electric-field control of nonvolatile magnetization in $Co_{40}Fe_{40}B_{20}/Pb(Mg_{1/3}Nb_{2/3})_{0.7}Ti_{0.3}O_3$ structure at room temperature, Phys. Rev. Lett. 108 (2012) 137203.
[26] T. Wu, A. Bur, P. Zhao, K.P. Mohanchandra, K. Wong, K.L. Wang, C.S. Lynch, G.P. Carman, Giant electric-field-induced reversible and permanent magnetization reorientation on magnetoelectric Ni/(011) [Pb(Mg1/3Nb2/3)O3](1-x)-[PbTiO3]x heterostructure, Appl. Phys. Lett. 98 (2011) 012504.
[27] M. Liu, B.M. Howe, L. Grazulis, K. Mahalingam, T.X. Nan, N.X. Sun, G.J. Brown, Voltage-impulse-induced non-volatile ferroelastic switching of ferromagnetic resonance for reconfigurable magnetoelectric microwave devices, Adv. Mater. 25 (2013) 4886–4892.
[28] Jiaping Han, Wenwu Cao, Electric field effects on the phase transitions in (001)-oriented (1-x)Pb(Mg1/3Nb2/3)O3-xPbTiO3 single crystals with compositions near the morphotropic phase boundary, Phys. Rev. B 68 (2003) 134102.
[29] M. Shanthi, L.C. Lim, Electric-field and stress-induced R-O phase transformation in [011]-poled $Pb(Mg1/3Nb2/3)O_3$–(28–32)% $PbTiO_3$ single crystals of [100]-length cut, J. Appl. Phys. 106 (2009) 114116.
[30] Y. Ohtani, I. Hatakeyama, Antiferro-ferromagnetic transition and microstructural properties in a sputter deposited FeRh thin film system, J. Appl. Phys. 74 (1993) 3328–3332.
[31] B. Noheda, D.E. Cox, G. Shirane, J. Gao, Z.G. Ye, Phase diagram of the ferroelectric relaxor (1-x)$PbMg_{1/3}Nb_{2/3}O_3$-x$PbTiO_3$, Phys. Rev. B 66 (2002) 054104.
[32] J. Narayan, B.C. Larson, Domain epitaxy: a unified paradigm for thin film growth, J. Appl. Phys. 93 (2003) 278.
[33] W. Zhang, Y. Li, L.J. Wu, Y.D. Duan, K. Kisslinger, C.L. Chen, D.C. Bock, F. Pan, Y.M. Zhu, A.C. Marschilok, E.S. Takeuchi, K.J. Takeuchi, F. Wang, Multi-electron transfer enabled by topotactic reaction in magnetite, Nat. Commun. 10 (2019) 1972.
[34] J.M. Titchmarsh, Comparison of high spatial resolution in EDX and EELS analysis, Ultramicroscopy 28 (1989) 347–351.
[35] M.I. Aivazov, O.M. Morozova, I.A. Domashnev, Synthesis and investigation of alloys in the systems tio-mgo and vo-mgo, Inorg. Mater. (translated from Neorganicheskie Materialy) 10 (1974) 1637–1638.
[36] M.C. Dekker, A. Herklotz, L. Schultz, M. Reibold, K. Vogel, M.D. Biegalski, H.M. Christen, K. Dörr, Phys. Rev. B 84 (2011) 054463.
[37] Z. Liu, Z. Feng, H. Yan, X. Wang, X. Zhou, P. Qin, H. Guo, R. Yu, C. Jiang, Antiferromagnetic piezospintronics, Adv. Electron. Mater. 5 (2019) 1900176.
[38] Z.Q. Liu, L. Li, Z. Gai, J.D. Clarkson, S.L. Hsu, A.T. Wong, L.S. Fan, M.W. Lin, C.M. Rouleau, T.Z. Ward, H.N. Lee, A.S. Sefat, H.M. Christen, R. Ramesh, Full electroresistance modulation in a mixed-phase metallic alloy, Phys. Rev. Lett. 116 (2016) 097203.
[39] R.O. Cherifi, V. Ivanovskaya, L.C. Phillips, A. Zobelli, I.C. Infante, E. Jacquet, V. Garcia, S. Fusil, P.R. Briddon, N. Guiblin, A. Mougin, A.A. Ünal, F. Kronast, S. Valencia, B. Dkhil, A. Barthélémy, M. Bibes, Electric-field control of magnetic order above room temperature, Nat. Mater. 13 (2014) 345–351.
[40] Y. Liu, Y.G. Zhao, P.S. Li, S. Zhang, D.L. Li, H. Wu, A.T. Chen, Y. Xu, X.F. Han, S.Y. Li, D. Lin, H.S. Luo, Electric-field control of magnetism in $Co_{40}Fe_{40}B_{20}$/(1-x)Pb(Mg1/3Nb2/3)O_3-x$PbTiO_3$ multiferroic heterostructures with different ferroelectric phases, ACS Appl. Mater. Interfaces 8 (2016) 3784.
[41] G.C. Han, J.J. Qiu, Q.J. Yap, P. Luo, T. Kanbe, T. Shige, D.E. Laughlin, J.G. Zhu, Suppression of low-temperature ferromagnetic phase in ultrathin FeRh films, J. Appl. Phys. 113 (2013) 123909.
[42] I. Suzuki, T. Koike, M. Itoh, T. Taniyama, T. Sato, Stability of ferromagnetic state of epitaxially grown ordered FeRh thin films, J. Appl. Phys. 105 (2009) 07E501.
[43] R. Fan, C.J. Kinane, T.R. Charlton, R. Dorner, M. Ali, M.A. de Vries, R.M.D. Brydson, C.H. Marrows, B.J. Hickey, D.A. Arena, B.K. Tanner, G. Nisbet, S. Langridge, Ferromagnetism at the interfaces of antiferromagnetic FeRh epilayers, Phys. Rev. B 82 (2010) 184418.
[44] M. Loving, F. Jimenez-Villacorta, B. Kaeswurm, D.A. Arena, C.H. Marrows, L.H. Lewis, Structural evidence for stabilized ferromagnetism in epitaxial FeRh nanoislands, J. Phys. D Appl. Phys. 46 (2013) 162002.
[45] L. Caron, Z.Q. Ou, T.T. Nguyen, D.T. CamThanh, O. Tegus, E. Bruck, On the determination of the magnetic entropy change in materials with first-order transitions, J. Magn. Magn. Mater. 321 (2009) 3559–3566.
[46] K.A. Gschneidner Jr, V.K. Pecharsky, A.O. Pecharsky, C.B. Zimm, Recent developments in magnetic refrigeration, Mater. Sci. Forum 315 (317) (1999) 69–76.
[47] L.D. Griffith, Y. Mudryk, J. Slaughter, V.K. Pecharsky, Material-based figure of merit for caloric materials, J. Appl. Phys. 123 (2018) 034902.
[48] M. Shanthi, S.M. Chia, L.C. Lim, Overpoling resistance of [011]-poled $Pb(Mg1/3Nb2/3)O_3$–$PbTiO_3$ single crystals, Appl. Phys. Lett. 87 (2005) 202902.
[49] S.L. Russek, C.B. Zimm, Potential for cost effective magnetocaloric air conditioning systems, Int. J. Refrig. 29 (2006) 1366–1373.
[50] V.K. Pecharsky, K.A. Gschneidner Jr., Tunable magnetic regenerator alloys with a giant magnetocaloric effect for magnetic refrigeration from 20 to 290K, Appl. Phys. Lett. 70 (1997) 3299–3301.